cm CHEMISTRY OF MATERIALS
Article
Cite This: Chem. Mater. 2019, 31, 2431−2442
pubs.acs.org/cm

Computational Investigation and Experimental Realization of Disordered High-Capacity Li-Ion Cathodes Based on Ni Redox

Huiwen Ji,[†,§,‡] Daniil A. Kitchaev,[∥,‡] Zhengyan Lun,[†,§] Hyunchul Kim,[§] Emily Foley,[⊥] Deok-Hwang Kwon,[†,§] Yaosen Tian,[†,§] Mahalingam Balasubramanian,[#] Matteo Bianchini,[§] Zijian Cai,[†,§] Raphaële J. Clément,[⊥] Jae Chul Kim,[§,∇] and Gerbrand Ceder[*,†,§]

[†]Department of Materials Science and Engineering, University of California Berkeley, Berkeley, California 94720, United States
[§]Materials Sciences Division, Lawrence Berkeley National Laboratory, Berkeley, California 94720, United States
[∥]Department of Materials Science and Engineering, Massachusetts Institute of Technology, Cambridge, Massachusetts 02139, United States
[⊥]Materials Department, University of California Santa Barbara, Santa Barbara, California 93106, United States
[#]X-Ray Science Division, Advanced Photon Source, Argonne National Laboratory Argonne, Lemont Illinois 60439, United States
[∇]Department of Chemical Engineering and Materials Science, Stevens Institute of Technology, Hoboken, New Jersey 07030, UnitedStates

Supporting Information

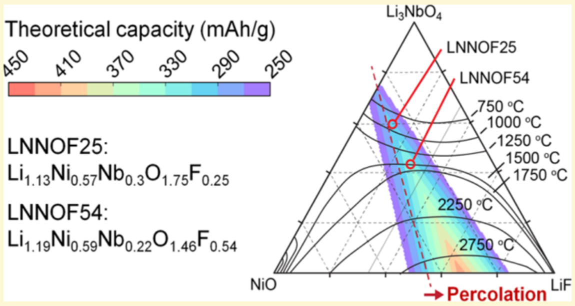

ABSTRACT: In cation-disordered rocksalt Li-ion cathode materials, an excess of Li with respect to the transition metal content is necessary for the creation of percolating pathways for Li transport. Because of the lower amount of redox-active transition metal, a substantial part of the charge transfer must occur via less reversible oxygen redox. Fluorination can be used to minimize this dependence on oxygen redox by increasing the amount of low-valent transition metal in the compound, but it adds complexity to materials design. Here, we investigate the feasibility of using computationally constructed phase diagrams to facilitate the search for optimal oxyfluorides. We use the phase diagram of $LiF-Li_3NbO_4-NiO$ to identify $Li_{1.13}Ni_{0.57}Nb_{0.3}O_{1.75}F_{0.25}$ and $Li_{1.19}Ni_{0.59}Nb_{0.22}O_{1.46}F_{0.54}$ as two promising compositions and demonstrate that they can be successfully synthesized. These compounds exhibit significantly reduced hysteresis and higher energy density than the previously reported $Li_{1.3}Ni_{0.27}Nb_{0.43}O_2$ compound in this space. Although we generally attribute the improved performance to the increased Ni content enabled by fluorination, a more nuanced relation between fluorination and the cycling behavior is revealed through electrochemical tests, X-ray absorption spectroscopy, solid-state nuclear magnetic resonance spectroscopy, and density functional theory. We find that fluorination increases the voltage, improves cycle life, but reduces the accessibility of Ni redox. Consideration of these effects will facilitate the future design of optimized disordered-rocksalt oxyfluoride cathodes.

■ INTRODUCTION

The recently discovered Li-excess cation-disordered rocksalt (DRX) structures offer several advantages over traditional layered materials as Li-ion cathodes. Without a constraint on the cation order, DRX materials form with various chemistries, enabling the design of cathodes based on a wide range of redox-active transition metals (TMs) and non-redox-active stabilizers, including earth-abundant elements such as Fe, Mn, and Ti.[1−4] Importantly, Li transport is controlled by the presence of a percolating network of Li-rich environments (i.e., 0-TM channels) rather than by any well-defined channels and persists even when the lattice undergoes significant structural rearrangement.[5,6] However, optimizing DRX cathodes for energy density and reversibility presents a formidable challenge because of the diversity of structural and chemical environments, which fundamentally alter the electrochemical behavior of the materials.

The necessity of Li excess to form a percolating Li network in DRXs inevitably reduces the amount of redox-active TM, resulting in a significant dependence on oxygen redox to deliver high capacity. Although oxygen redox can provide this extra capacity, the concomitant oxygen loss and lattice densification[1] associated with this process lead to limited reversibility.[7,8] One approach to address this irreversibility is through fluorination. In contrast to layered Li−TM oxides, Li-excess DRXs are readily fluorinated as they contain anion sites coordinated by five or six Li, which have a low F incorporation

Received: December 9, 2018
Revised: March 12, 2019
Published: March 26, 2019

DOI: 10.1021/acs.chemmater.8b05096
Chem. Mater. 2019, 31, 2431−2442

energy.[9] F substitution decreases the average anion valence and thus allows for the presence of more low-valent redox-active cations and even double-redox couples such as $Mn^{2+/4+}$ and $V^{3+/5+}$.[10−12] Furthermore, fluorination appears to be effective in suppressing oxygen loss, as a number of heavily fluorinated Li cathodes, for example, $Li_2Mn_{1/2}Ti_{1/2}O_2F$, $Li_2Mn_{2/3}Nb_{1/3}O_2F$, and Li_2MnO_2F, have been shown to exhibit negligible oxygen evolution even when charged to 4.8 or 5 V.[13,14] Nonetheless, the mechanism by which F affects performance has not yet been fully established.

With fluorination as a new degree of freedom to tune the average anion and cation valence, the rational design of DRX cathodes becomes increasingly complex, requiring careful balance between the Li-excess level and TM content as well as consideration of a feasible fluorination level and synthesis temperature. Fluorination requires Li-rich local environments, which are prone to phase segregation into LiF; thus, a high temperature is generally needed to ensure sufficient miscibility to form a single-phase disordered structure.[9]

In this study, we computationally identify two Ni-based oxyfluorides in the $LiF-Li_3NbO_4-NiO$ system optimized for maximum TM capacity at different levels of fluorination. We successfully synthesize and experimentally characterize both materials and find that the oxidation of Ni^{2+} provides capacity at a high voltage, yielding a specific energy of up to 765 Wh/kg in the first discharge. This performance is superior to that of a previously reported non-fluorinated material in this space but still does not reach the theoretically predicted performance level. We find that the primary obstacle to realizing the theoretical energy density is that Ni redox rapidly becomes competitive with oxygen redox, even at a relatively low Ni oxidation state. We attribute this limit in the accessibility of highly oxidized Ni to the large number of Ni−F bonds and the generally large Ni−O bond length in these materials.

■ EXPERIMENTAL SECTION

Synthesis. For the synthesis of $Li_{1.13}Ni_{0.57}Nb_{0.3}O_{1.75}F_{0.25}$ (LNNOF25) and $Li_{1.19}Ni_{0.59}Nb_{0.22}O_{1.46}F_{0.54}$ (LNNOF54), stoichiometric NiO, Nb_2O_5, LiF, and 5% excess Li_2O with a total amount of 2 g each were dispensed into 50 mL stainless-steel jars. The jars were sealed with safety closure clamps in an Ar-filled glovebox. LNNOF25 and LNNOF54 were synthesized by mechanical alloying using a planetary ball mill (Retsch PM200) at a rotating rate of 450 rpm. The ball-to-powder weight ratio was 20:1. The milling process was paused every 20−30 h, and X-ray diffraction (XRD) patterns of the intermediate products were obtained. The milling was continued until the XRD pattern showed a good fit with the expected structural model. The total milling times for LNNOF25 and LNNOF54 were 180 and 160 h, respectively. Based on our experience with the ball milling method, the milling time is affected by the stability and the particle size of precursors.

Characterization and Electrochemistry. The XRD patterns were obtained using a Rigaku MiniFlex 600 diffractometer equipped with a Cu source. Rietveld refinement was performed using the HighScore Plus software package. Scanning electron microscopy (SEM) images were obtained on a Zeiss Gemini Ultra-55 analytical field-emission scanning electron microscope. Energy-dispersive X-ray spectroscopy (EDS) elemental mapping was performed using a JEOL JEM-2100F microscope equipped with an X-max EDS detector. To fabricate the electrodes, the active material (70 wt %) was manually mixed with Super C65 carbon black (Timcal, 20 wt %) in a mortar inside an Ar-filled glovebox, followed by mixing with polytetrafluoroethylene (DuPont, 10 wt %). The mixture was then rolled into a thin film for use as the cathode. A 2032 type coin cell was assembled using 1 M $LiPF_6$ (in a volumetric 1:1 mixture of ethylene carbonate and dimethyl carbonate), glass microfiber filters (grade GF/F, Whatman), and Li metal foil (FMC) as the electrolyte, separator, and anode, respectively. The coin cells were tested on an Arbin BT-2000 battery testing station. The energy density of each material was calculated by integrating the discharge voltage profile versus the capacity. The average voltage was then obtained by dividing the energy density by the specific capacity.

Solid-State Nuclear Magnetic Resonance Spectroscopy (ssNMR). ^{19}F and ^{7}Li NMR data were collected on both LNNOF25 and LNNOF54 powders before and after annealing using a Bruker Avance 500 MHZ (11.7 T) wide-bore NMR spectrometer with Larmor frequencies of −470.6 and −194.4 MHz, respectively, at room temperature. The data was obtained using 60 kHz magic-angle spinning (MAS) with a 1.3 mm double-resonance probe. ^{19}F and ^{7}Li NMR data were referenced to lithium fluoride (LiF, $\delta(^{19}F) = -204$ ppm and $\delta(^{7}Li) = -1$ ppm). ^{19}F spin echo spectra were acquired on all samples using a 90° RF pulse of 1.0 μs and a 180° RF pulse of 2.0 μs at 76.3 W. A recycle delay of 14 s was used for LiF, while a recycle delay of 50 ms was used for the LNNOF25 and LNNOF54 samples. Additionally, ^{19}F pj-MATPASS (projected magic-angle turning phase-adjusted sideband separation)[15] isotropic spectra were acquired on LNNOF25 and LNNOF54 samples using a 90° RF pulse of 1.0 μs at 76.3 W with a recycle delay of 50 ms. A ^{19}F background spectrum, also obtained on the empty probe using the same conditions as the LNNOF25/LNNOF54 spin echo spectra, showed no significant background signal. ^{7}Li spin echo spectra were also acquired on all samples using a 90° RF pulse of 0.7 μs and a 180° RF pulse of 1.4 μs at 110 W with a recycle delay of 14 s for LiF and 500 ms for all other samples. ^{7}Li pj-MATPASS isotropic spectra were also acquired on the LNNOF25 and LNNOF54 samples using a 90° RF pulse of 0.7 μs at 110 W with a recycle delay of 500 ms. Lineshape analysis was carried out within the Bruker Topspin software using the SOLA lineshape simulation package.

X-ray Absorption Spectroscopy. Ex situ X-ray absorption spectroscopy (XAS) measurements were conducted in transmission mode at room temperature using beamline 20-BM at the Advanced Photon Source (APS) at Argonne National Laboratory. The prepared XAS samples were sealed with polyimide tape (Kapton, DuPont) to prevent air exposure. The incident energy was selected using a Si(111) monochromator. The energy calibration was performed by simultaneously measuring the spectra of Ni or Nb metal foils. Harmonic rejection was accomplished using a Rh-coated mirror. Data preprocessing operations including deglitching, energy calibration, normalization, and least-squares fitting with theory were performed as described by Kelly et al.[16] using IFEFFIT[17] with an FEFF code.[18] The extracted extended X-ray absorption fine structure (EXAFS) signal $\chi(k)$ was weighted by k^3 to emphasize the high-energy oscillation and then Fourier-transformed in a k-range from 3.0 to 12.8 Å^{-1} for the Ni K-edge and from 3.0 to 10.3 Å^{-1} for the Nb K-edge using a Hanning window to obtain magnitude plots of the EXAFS spectra in R-space.

DFT Calculations. All DFT calculations were performed using the Vienna ab initio simulation package (VASP)[19,20] using the projector-augmented wave method,[21] a plane-wave basis set with an energy cutoff equal to 520 eV, and a reciprocal space discretization of 25 K-points per Å^{-1}. All calculations were converged to 10^{-5} eV in total energy and 20 meV/Å in interatomic forces. Following the methodology described in our previous report,[12] we relied on several functionals for various aspects of the analysis. To construct the phase diagram of the $NiO-Li_3NbO_4-LiF$ space on a fully lithiated rocksalt lattice, we relied on the exchange-correlation functional of Perdew, Burke, and Ernzerhof[22] supplemented with a Hubbard-U correction[23] to offset the effect of the self-interaction error. The selected values of U (6 eV for Ni, 1.5 eV for Nb) were based on the calibration of oxide formation energies reported by Jain et al.[24] To identify favorable Li-vacancy configurations at various states of charge, we relied on the SCAN functional that provides a superior representation of the relative stability of structures at the same chemical composition.[25,26] Finally, to evaluate the voltage curve and redox configuration of our materials at various states of charge, we used the Heyd−Scuseria−

DOI: 10.1021/acs.chemmater.8b05096
Chem. Mater. 2019, 31, 2431−2442

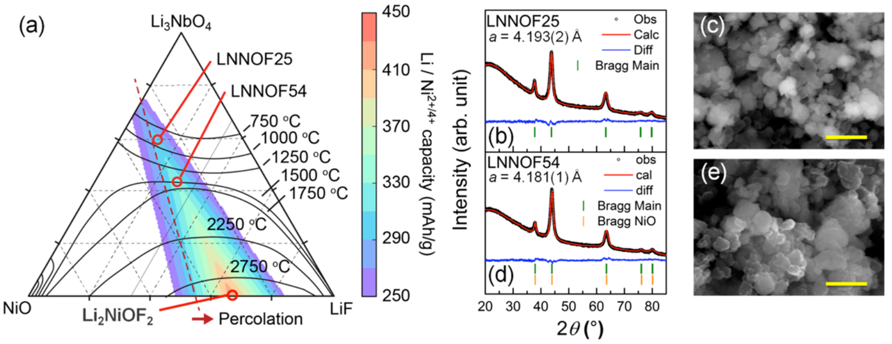

Figure 1. (a) Computed phase diagram and theoretical capacity of the Li_3NbO_4−NiO−LiF system, constrained to solid phases on a rocksalt lattice. The temperature contours denote the extent of the binodal at the marked temperature, starting from the NiO and Li_3NbO_4 endpoints. The color-coded overlay maps the minimum of the theoretical Li and $Ni^{2+/4+}$ gravimetric capacity, and the red dashed lines represent compositions with at least 9% Li excess required for percolative Li transport. (b−e) Structural and morphological characterization of LNNOF25 and LNNOF54. Room-temperature XRD patterns and Rietveld refinement results of (b) LNNOF25 and (d) LNNOF54. SEM images of (c) LNNOF25 and (e) LNNOF54 after manually mixing with carbon black (scale bars, 200 nm).

Ernzerhof functional.[27] VASP input and output processing was performed using the Python Materials Genomics package.[28]

Cluster Expansion. We utilized cluster expansion Hamiltonians[29] to parametrize independently of each other the configurational energies of Li, Ni, Nb, O, and F on a dense rocksalt lattice and the energies of Li-vacancy arrangements in a partially delithiated DRX structure. This methodology precisely follows the procedure described by Kitchaev et al.[12] for characterizing the synthesis and electrochemical behavior of Li−Mn−V−O−F DRXs. Simultaneous disorder on the anion and cation lattice can be included following the coupled cluster expansion approach of Tepesch et al.[30] In both cases, we parametrized the cluster expansions using approximately 400 lattice configurations computed within DFT, using a basis set of pair interactions up to 7 Å, triplet interactions up to 4.1 Å, and quadruplet interactions up to 4.1 Å, with respect to a rocksalt primitive cell with a lattice constant a of 3 Å. In all cases, the interactions were taken as deviations from a baseline of formal-charge electrostatics and a fitted dielectric constant.[9] The effective cluster interactions and dielectric constant were obtained from a L_1-regularized linear regression fit, with the regularization parameter optimized by cross-validation.[31] The resulting fits yielded errors of 6 and 4 meV/atom for the dense rocksalt and Li-vacancy cluster expansions, respectively. All canonical Monte Carlo simulations based on these Hamiltonians were run using the Metropolis−Hastings algorithm.

■ RESULTS

Computational Design. The thermodynamic stability of the DRXs in the NiO−Li_3NbO_4−LiF space is first evaluated to estimate the synthetic accessibility of various compositions. Following the methodology reported previously for evaluating the synthesizability of a mixed-TM oxyfluoride,[12] we compute the NiO−Li_3NbO_4−LiF ternary phase diagram. Note that we restrict our analysis to solid phases on the rocksalt lattice, explicitly neglecting molten and vapor phases, which is sufficient for our qualitative analysis but limits the general applicability of the computed phase diagram. The phase diagram, shown in Figure 1a, is plotted using temperature−composition contours that map the extent of the binodal at the designated temperature, starting from the NiO or Li_3NbO_4 endpoint. The contours closely map the range of compositions that would be accessible using a near-thermodynamic synthesis method such as solid-state sintering. However, in our work, we rely on mechanochemical synthesis, the outcome of which does not have a known rigorous mapping to thermodynamic quantities. We thus follow previous successful synthesis examples[12,14] to heuristically assign the 1750 °C contour as the upper limit for synthetic accessibility. While this choice of upper bound on accessible temperature is purely heuristic, based on our prior observations of what can be made, we speculate that it corresponds to a point above which the driving force for decomposition begins to overcome kinetic barriers and yields a large enough de-mixing rate to dwarf the mixing effect induced by ball milling.

We evaluate several design criteria for a DRX cathode to identify compositions with good electrochemical properties. First, at least 9% Li excess is required to form a percolating network of Li conductive channels in DRXs.[5] In Figure 1a, the compositions satisfying this criterion lie to the right of the red dashed lines. Second, we aim to maximize the expected capacity. The colored regions overlaid on the phase diagram in Figure 1a indicate the theoretical capacity calculated based on the minimum of the Li capacity and the theoretical Ni capacity (assuming complete Ni^{2+} to Ni^{4+} oxidation). High fluorine content is clearly favorable, as compositions approaching the disordered Li_2NiOF_2 endpoint have the highest theoretical capacity. However, these compositions only appear to be accessible at an unreasonably high temperature, signifying that they are unlikely to be synthetically accessible or to resist phase separation post-synthesis. Considering the previously mentioned constraints on synthesizability, we identify the composition with maximal theoretical capacity for each of two synthesis temperatures: $Li_{1.13}Ni_{0.57}Nb_{0.3}O_{1.75}F_{0.25}$ (LNNOF25), which becomes stable near 1000 °C, and $Li_{1.19}Ni_{0.59}Nb_{0.22}O_{1.46}F_{0.54}$ (LNNOF54), which lies near the 1750 °C heuristic synthesizability limit. The theoretical Li capacity (balanced with Ni^{2+}/Ni^{4+} capacity) of LNNOF25 is 296 mAh/g while that of LNNOF54 is 327 mAh/g. These two materials have sufficient Li excess, balanced Li and Ni theoretical capacities, and are likely to be synthesizable but differ in their degree of fluorination and overall stability, forming the basis of our case study into the effect of fluorine content on Ni electrochemistry in a DRX.

Synthesis, Characterization, and Electrochemical Performance. We successfully synthesized LNNOF25 and LNNOF54 using planetary ball milling. The final XRD patterns are presented in Figure 1b,d. Both materials form in a DRX structure with no detectable impurity peaks. The Rietveld refinement results indicate good agreement between the experimental observation and the calculation based on a simple rocksalt structural model. The lattice parameters of

DOI: 10.1021/acs.chemmater.8b05096
Chem. Mater. 2019, 31, 2431−2442

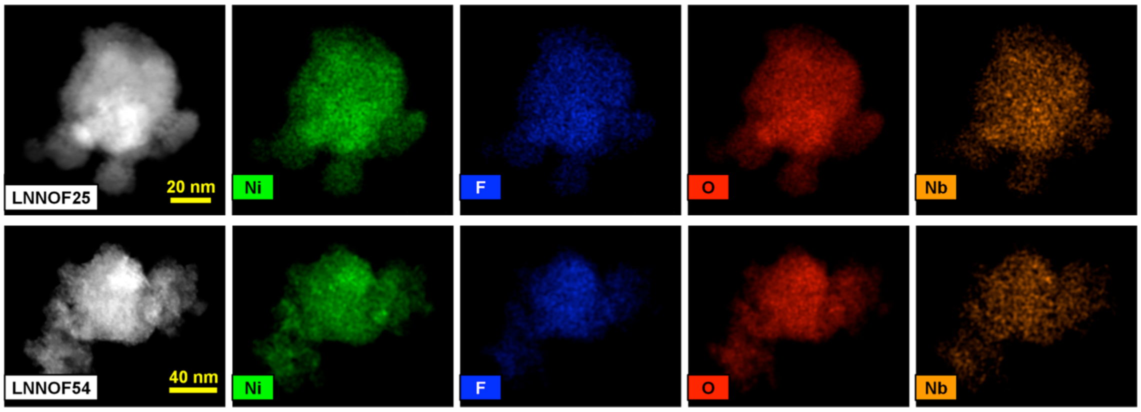

Figure 2. EDS elemental mappings of as-ball-milled LNNOF25 (top row) and LNNOF54 particles (bottom row).

LNNOF25 and LNNOF54 are refined to be 4.193(2) and 4.181(1) Å, respectively. Given that one of the precursors, NiO, has the same crystal structure as the DRXs and a comparable lattice parameter (4.177 Å),[32] we include it as a possible impurity phase in the Rietveld refinement. Although the XRD pattern of LNNOF25 shows a good fit with 100% of the target phase, that of LNNOF54 is refined to contain 2.3% NiO and 97.7% of the DRX phase. SEM images of LNNOF25 and LNNOF54 particles manually mixed with carbon black are presented in Figure 1c,e. The average primary particle size is estimated to be between 100 and 200 nm. We note that even a single primary particle has multiple crystallites in it.

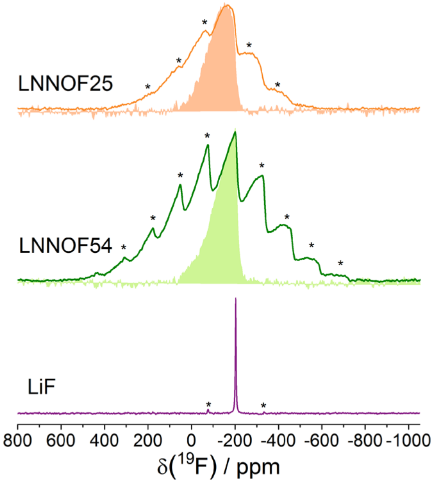

Figure 3. ^{19}F spin echo NMR spectra obtained at 60 kHz MAS for LNNOF25 (orange, top), LNNOF54 (green, middle), and LiF (purple, bottom). Spinning sidebands in the spin echo spectra are labeled with asterisks. The shaded areas in the top and middle spectra correspond to ^{19}F pj-MATPASS isotropic spectra collected on LNNOF25 and LNNOF54 and indicate the presence of broad, overlapping signals spanning a wide range of resonant frequencies. The spectra obtained on LNNOF25 and LNNOF54 are scaled according to the number of scans in the experiment and the amount of sample in the NMR rotor.

To study the compositional homogeneity of the as-ball-milled samples, scanning TEM/EDS mapping is performed, and the results are presented in Figure 2. Uniform distributions of all the elements are observed for both materials. To further prove the bulk substitution of fluorine, ^{19}F ssNMR experiments are performed on LNNOF25 and LNNOF54 to study the local chemical environments of fluorine. If fluorine exists in a segregated LiF phase, then the ^{19}F NMR data are expected to show a sharp peak at −204 ppm, as shown for the bottom spectrum in Figure 3. On the contrary, if fluorine is incorporated into the targeted DRX phase, then a wide variety of chemical environments are expected. ^{19}F spin echo and pj-MATPASS spectra collected for the two compounds are shown in Figure 3. Both materials show signals that span a wide range of chemical shift, as evidenced from the pj-MATPASS data (shaded areas in the top and middle spectra), indicating the presence of various local environments of fluorine. The significant broadening of the peaks also suggests that the fluorine ions are in close proximity (<5 Å) to paramagnetic ions (Ni^{2+} in this case). Specifically, the pj-MATPASS spectrum of LNNOF25 shows a broad peak centered around −155 ppm, with a slight asymmetry toward −204 ppm, suggesting the close to complete F integration in the bulk of the material, with only a small proportion of F nuclei in LiF-like environments. The pj-MATPASS spectrum of LNNOF54 shows a slightly higher signal intensity at −204 ppm than that of LNNOF25. These observations confirm that the majority of F ions in both materials are incorporated into the paramagnetic DRX phases with the low-F substituted LNNOF25 containing almost no LiF and the high-F substituted LNNOF54 containing a small amount of LiF. The exact quantification of LiF-like environments in these compounds is complicated by the ambiguous multicomponent fit of the broad, overlapping peaks in the spin echo spectra, as well as the absence of the signal from F nuclei directly bonded to Ni, as discussed in previous studies.[10,12,14,33]

The first-cycle voltage profiles of LNNOF25 and LNNOF54 for different voltage windows are presented in Figure 4a,b, respectively. Both materials exhibit much smaller hysteresis than that of a previously reported oxide analogue, $Li_{1.3}Ni_{0.27}Nb_{0.43}O_2$.[2] Specifically, after the first charge to 4.8 V, the discharge capacities above 3 V are 149 and 157 mAh/g for LNNOF25 and LNNOF54, respectively, whereas that for the unfluorinated $Li_{1.3}Ni_{0.27}Nb_{0.43}O_2$ is less than 50 mAh/g.[2] The voltage profiles of the two oxyfluorides also differ. LNNOF54 has a slightly higher voltage than LNNOF25. Consequently, when cycled between 1.5 and 4.6 V, the discharge capacity of LNNOF54 (215 mAh/g, 671 Wh/kg) is slightly smaller than that of LNNOF25 (221 mAh/g, 674 Wh/kg). However, when charged beyond 4.6 up to 4.8 V, the voltage of LNNOF25 increases faster than that of LNNOF54, resulting in a smaller capacity increase upon discharge for

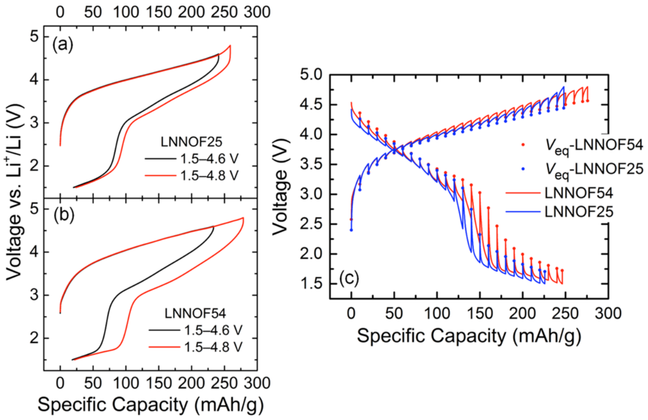

Figure 4. Electrochemical characterization of LNNOF25 and LNNOF54. First-cycle galvanostatic profiles of (a) LNNOF25 and (b) LNNOF54 at 20 mA/g between 1.5 and 4.6 V (black) and between 1.5 and 4.8 V (red). (c) First-cycle charge and discharge profiles during GITT measurement of LNNOF25 (blue) and LNNOF54 (red). The charge and discharge rate is 20 mA/g. After each step of 10 mA·h/g, the cell is relaxed for 5 h, and the resulting voltage−time response is recorded.

LNNOF25 to 235 mAh/g (713 Wh/kg) than for LNNOF54 to 257 mAh/g (765 Wh/kg).

To study the origin of the different voltage profiles of LNNOF25 and LNNOF54, the galvanostatic intermittent titration technique (GITT) is applied. Figure 4c presents the first-cycle voltage profiles between 1.5 and 4.8 V. The quasiequilibrium voltage (marked by dots) of LNNOF54 is slightly higher than that of LNNOF25. In addition, more significant polarization is observed for LNNOF25 than for LNNOF54 toward the upper cutoff voltage during charge. The most significant polarization for both materials, however, is observed at the end of discharge, a phenomenon that has been previously observed in $Li_{1.2}Ni_{1/3}Ti_{1/3}Mo_{2/15}O_2$.[1] We thus expect a similar mechanism of in situ surface impedance buildup in our materials.

The rate capability is measured for each material, with a fresh cell for each rate test so that the interference from capacity fading is minimized. For each test, the cell is first charged to 4.4 V at a rate of 20 mA/g, followed by holding at 4.4 V for 2 h to ensure an equivalent point of charge, and then discharged at one of the selected rates of 20, 40, 100, 200, and 400 mA/g. The rate capability is observed to be slightly better for LNNOF54 than for LNNOF25 (Figure 5). As the discharge rate increases from 20 to 400 mA/g, the capacity of LNNOF25 decreases by 31% from 207 to 142 mAh/g, while that of LNNOF54 decreases by 16% from 173 to 145 mAh/g. Also, the discharge polarization observed in LNNOF54 is smaller than that in LNNOF25.

Redox Mechanism. We select LNNOF54 as a model system for which to study the redox mechanism using X-ray absorption near edge structure (XANES) measurements and DFT calculations.

The XAS analysis provides information about the redox and local environments around the two TM species, that is, Ni and Nb. Figure 6a presents the normalized Ni K-edge XANES spectra of LNNOF54 during the first cycle. Several representative states are selected including pristine, 167 mAh/g charged (167c, equivalent to the theoretical capacity of Ni^{2+}/Ni^{3+}), 280 mAh/g charged (280c), 176 mAh/g discharged (176dc), and 257 mAh/g discharged (257dc). NiO and $NaNi_{1/2}Co_{1/2}O_2$[34] are used as Ni^{2+} and Ni^{3+} standards, respectively. The Ni K-edge starts from an energy close to that of the Ni^{2+} standard and shifts toward but does not fully reach that of the Ni^{3+} standard when charged from the pristine to 167c state. No obvious shift is observed upon

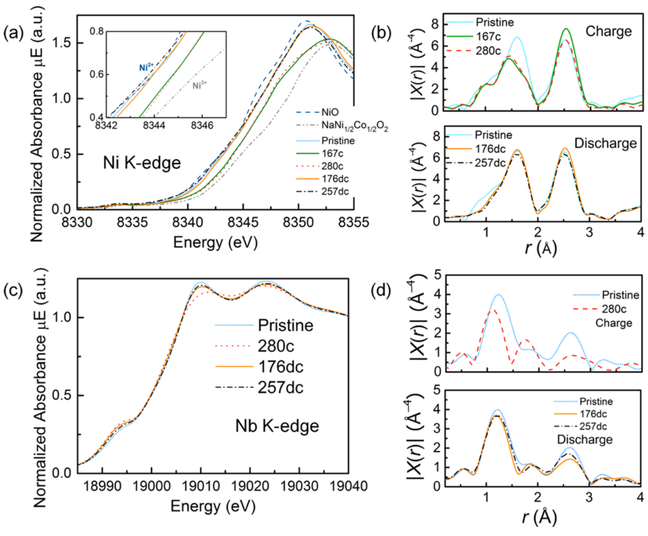

Figure 6. Normalized XANES spectra of (a) Ni K-edge and (c) Nb K-edge at selected states of charge and discharge within the first cycle. Their corresponding Fourier transform magnitudes of k^3-weighted EXAFS spectra are presented in panels (b) and (d), respectively.

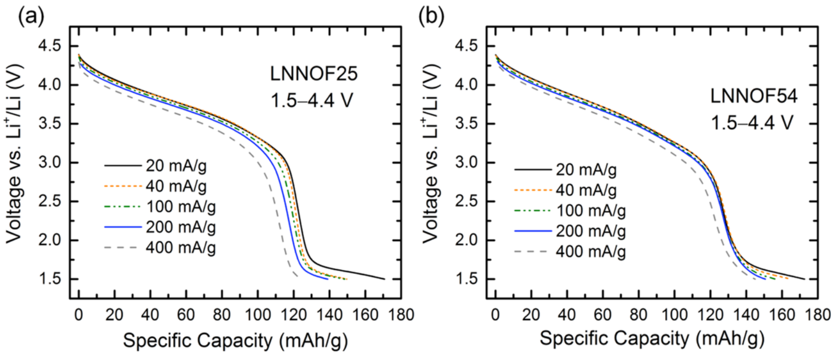

Figure 5. Discharge voltage profiles of (a) LNNOF25 and (b) LNNOF54 for the first cycle at various discharge rates of 20, 40, 100, 200, and 400 mA/g. For each test, the cell is charged to 4.4 V at a constant rate of 20 mA/g, followed by holding at 4.4 V for 2 h, before discharge.

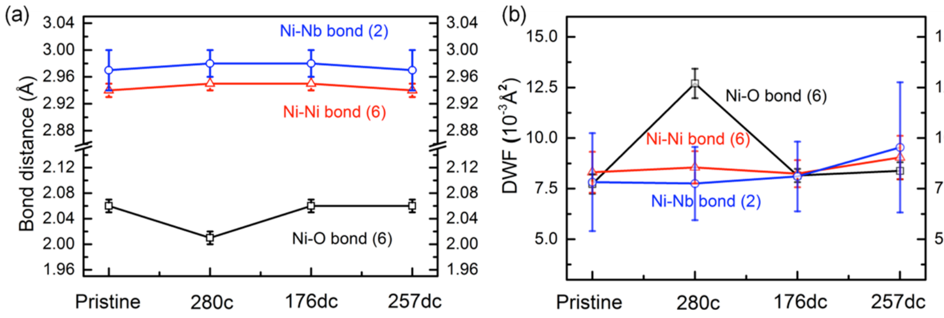

Figure 7. (a) Distances of the Ni−O, Ni−Ni, and Ni−Nb interactions within the first and second coordination shells from the quantitative analysis of the Fourier transform magnitudes of k^3-weighted Ni K-edge EXAFS spectra at various states of charge and discharge. (b) Debye−Waller factor associated with each bond type. The numbers in parentheses following bond names indicate the coordination numbers of various bond types.

further charge to 280c, suggesting that a different charge compensation mechanism, rather than the oxidation of Ni^{3+} to Ni^{4+}, is involved. During discharge, the position of the Ni K-edge recovers to that of the pristine state after discharge to 176dc, a state that coincides with a sharp voltage drop from 3 to 2 V. The Ni K-edge does not obviously shift below 2 V when further discharged to 257dc. Figure 6b shows the Fourier transform (FT) magnitudes of the k^3-weighted Ni K-edge EXAFS spectra. Upon charge to 280c, the Ni−O bond length noticeably decreases because of the oxidation of Ni^{2+} (r_{Ni2+} = 0.69 Å, r_{Ni3+} = 0.56 Å[35]), and any longer-range correlation beyond 3 Å is weakened. The EXAFS spectra fully recover to those of the pristine state after the completion of discharge, indicating that the local environment around Ni ions changes reversibly during the cycle.

The normalized Nb K-edge XANES spectra are presented in Figure 6c. During the cycle, the absorption edge barely shifts, indicating the absence of Nb redox. The slightly altered shapes of the XANES spectra originate from the distortion of the local environment[36] around Nb ions. The Nb K-edge EXAFS spectra are presented in Figure 6d. A single peak is observed in the pristine spectrum at ∼1.23 Å (phase uncorrected), which splits into two peaks after charge to 280c. This result suggests that the octahedral coordination around Nb ions is nearly symmetrical in the pristine state but distorts into having two distinct bond lengths at the top of charge. Such pronounced distortion around Nb ions is consistent with the recent finding that d^0 TM ions can distort to stabilize the DRX structure without a significant energy penalty.[37] Recovery of the EXAFS spectra at the Nb K-edge is also observed after a complete discharge.

The local environment around Ni ions is further investigated by refining the Ni K-edge EXAFS spectra at various states of charge and discharge, assuming no TM migration during cycling. The coordination numbers for the Ni−Ni (6) and Ni−Nb (2) bonds in the second coordination shell are used based on the stoichiometry of the compound. To avoid overfitting, we assume all the bonds of the same type within the same coordination shell have the same bond length. The refined structural parameters are plotted in Figure 7. More detailed crystallographic information obtained from this fit is provided in the Supporting Information. Figure 7a shows the Ni−O distances in the first coordination shell as well as the Ni−Ni and Ni−Nb interactions in the second coordination shell, at various states of charge and discharge.

From the pristine to the 280c state, the average Ni−O bond length decreases from 2.06(1) to 2.01(1) Å and then recovers to 2.06(1) Å after discharge to 176dc and 257dc. At the same time, the other bonds, that is, Ni−Ni and Ni−Nb, change negligibly during cycling. Figure 7b shows the Debye−Waller factor (DWF, i.e., mean square disorder) associated with each bond type. The DWF parameters are indicators of local distortion. From the pristine to 280c state, we observe a significant increase in local distortion in the Ni−O_6 shell, and such distortion is lifted upon discharge. This phenomenon is likely associated with the Jahn−Teller distortion of Ni^{3+} generated at the top of charge and is commonly observed in Ni-based cathode materials.[38] The DWF parameters of other bond types do not vary significantly during cycling.

The oxidation mechanism of LNNOF54 suggested by the XANES data is further corroborated using DFT calculations. We compute the voltage of $Li_{1.2-x}Ni_{0.6}Nb_{0.2}O_{1.4}F_{0.6}$, which is the closest composition we could achieve within the constraints of a computationally enumerable supercell (in this case, the lithiated composition $Li_{18}Ni_9Nb_3O_{21}F_9$ in a 5 × 3 × 2 supercell). To generate the approximate voltage profile of this disordered material, we follow the methodology described by Kitchaev et al.,[12] which assumes that (1) the energy of extracting any given Li from the cathode is determined by the local structure and Li content, (2) Li is always in equilibrium throughout the cathode, and (3) transition metal and anion rearrangement is limited to local coordination environment distortions. Briefly, we take 12 samples of $Li_{18}Ni_9Nb_3O_{21}F_9$ from a Monte Carlo simulation slightly above the binodal temperature and independently delithiate each one by finding optimal Li-vacancy configurations for each value of x. The lithiated sample structures are representative of local environments in the as-synthesized cathode, while their delithiation gives an estimate of the potential needed to extract Li from various regions of the material. We then construct the total voltage curve for $Li_{1.2-x}Ni_{0.6}Nb_{0.2}O_{1.4}F_{0.6}$ by adding the amount of Li, which can be extracted from each of the 12 sampled environments at a given voltage. The resulting voltage curve and the corresponding evolution of the Ni oxidation state are shown in Figure 8. Note that the deviation between the computed and measured voltages above 4.5 V and 50% delithiation ($x > 0.6$ Li/f.u.) originates from the dominance of oxygen oxidation in this region, as our calculations do not capture the significant structural rearrangements that often accompany a significant amount of oxygen oxidation. Indeed, the fact that the experimental curve in this region is lower than the calculated one supports the idea that O oxidation occurs with significant structural relaxation. Thus, we focus on the Ni-redox region of the voltage curve, where our DFT calculations provide a reasonable model of the oxidation process. Here, as x increases from 0 to 0.6 (i.e., the theoretical capacity of $Ni^{2+/3+}$),

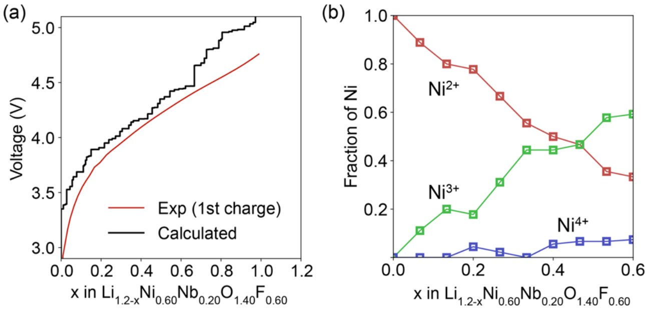

Figure 8. (a) Computed and experimental voltage profiles of LNNOF54. The calculation is based on a representative composition, $Li_{1.2}Ni_{0.6}Nb_{0.2}O_{1.4}F_{0.6}$ ($Li_{18}Ni_9Nb_3O_{21}F_9$), which is compatible with a computationally accessible supercell. (b) Evolution of Ni oxidation states at various states of charge up to $x = 0.6$, corresponding to the region where Ni redox is the most active source of electronic capacity, even though oxygen redox also contributes.

the fraction of Ni^{2+} decreases from 1.0 to ~0.35 and the fractions of Ni^{3+} and Ni^{4+} gradually increase to ~0.60 and ~0.05, respectively, following a stepwise oxidation of Ni^{2+} through Ni^{3+} intermediates, as demonstrated in a previous study on $Li_{1.15}Ni_{0.45}Ti_{0.3}Mo_{0.1}O_{1.85}F_{0.15}$.[33] These changes result in an effective increase in the Ni oxidation state from 2+ to ~2.7+. Thus, even in this early region of charge, Ni oxidation only accounts for 2/3 of the electron transfer, consistent with the observations from the Ni K-edge XANES spectra, where the detected oxidation state of Ni at 167c is between 2+ and 3+.

Using the combined XAS and DFT findings, we can propose a redox mechanism for LNNOF54. During charge, Ni^{2+} is first oxidized, but oxygen oxidation soon follows and gradually becomes the exclusive redox mechanism at high voltages. The oxidation state of Ni at 167c detected by XANES is less than 3+, indicating that a different charge compensation mechanism, that is, oxygen oxidation, is involved and overlaps with Ni oxidation. From 167c to 280c, the Ni K-edge barely shifts, suggesting the exclusive involvement of oxygen oxidation and/or oxygen loss. During discharge, Ni reduction and reversible lattice oxygen reduction first occur at high voltages, as the Ni K-edge at 176dc almost shifts back to the pristine position, while the Ni reduction only accounts for half of the delivered capacity. The extra capacity of ~80 mAh/g below 3 V cannot be attributed to Ni or Nb reduction. We suspect that this extra capacity originates from lattice oxygen, whose redox sometimes occurs asymmetrically during charge and discharge because of structural rearrangement during cycling.[39,40] The large voltage hysteresis of such as yet unidentified process is consistent with the significant polarization we observe in this region.

Capacity Retention and Effect of Annealing. The cyclability of the two materials is tested for 20 continuous cycles at 20 mA/g with a 1 min rest step between charge and discharge cycles. The voltage profiles for the first five cycles and their capacity evolution upon further cycles are shown in Figure 9. LNNOF54 exhibits better capacity retention than LNNOF25. For example, when cycled between 1.5 and 4.6 V, LNNOF25 only retains 40% of its initial capacity after 20 cycles, whereas LNNOF54 retains 78% of its initial capacity. In addition, upon cycling, a more pronounced polarization increase is observed for the voltage profile of LNNOF25 than that of LNNOF54. The polarization increase is indicated by a rise of the charge voltage and a decline of the discharge voltage. Finally, for both materials, during discharge, the low-voltage region below 2 V, which is associated with a pronounced polarization, evolves faster when charging to a higher upper cutoff voltage, consistent with the fact that oxygen loss and the subsequent surface densification are more significant at high voltages.

Given that mechanochemical synthesis often results in a considerable amount of local strain in the material structure,

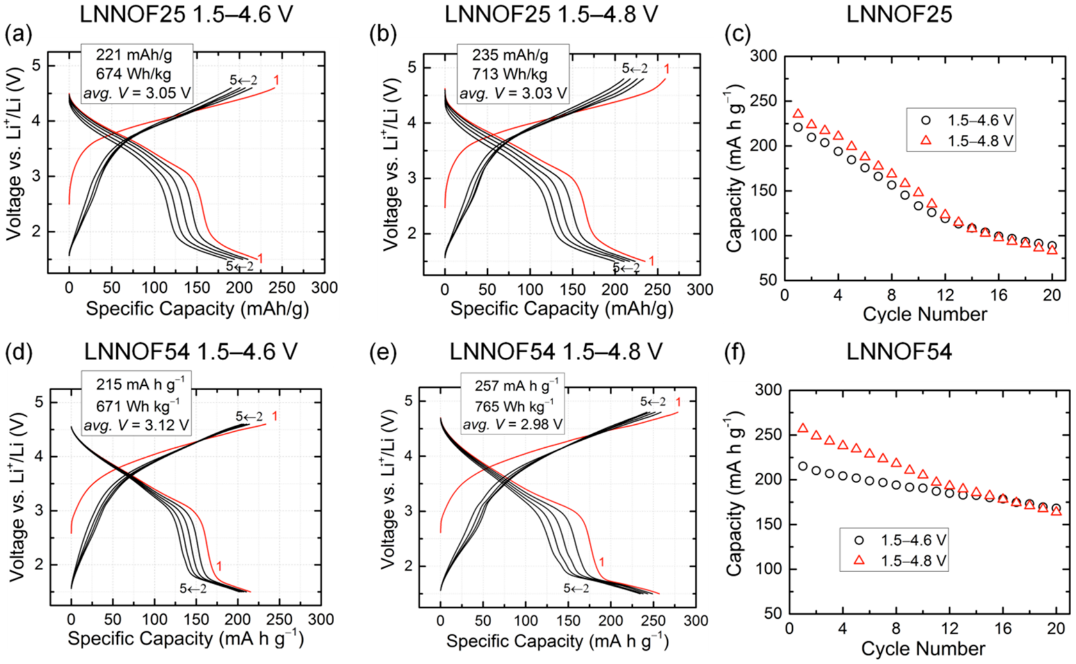

Figure 9. Capacity retention of as-ball-milled (a–c) LNNOF25 and (d–f) LNNOF54 within two different voltage windows, 1.5–4.6 and 1.5–4.8 V. The first-cycle discharge capacity, energy density, and average voltage are provided at the top of each diagram. The voltage profiles for the first 5 cycles and the capacity evolution over 20 cycles for LNNOF25 and LNNOF54 are shown. The cycling rate for all tests is 20 mA/g.

DOI: 10.1021/acs.chemmater.8b05096
Chem. Mater. 2019, 31, 2431–2442

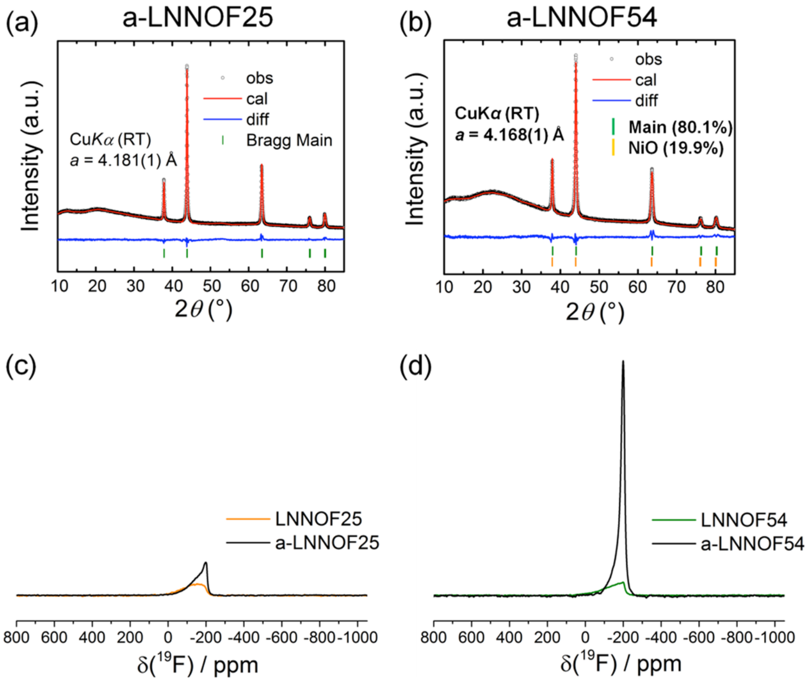

Figure 10. Room-temperature XRD patterns and Rietveld refinement results for (a) a-LNNOF25 and (b) a-LNNOF54. ^{19}F pj-MATPASS isotropic NMR spectra of LNNOF25 (c) and LNNOF54 (d) before and after annealing. The spectra are scaled according to the number of scans in the experiment and the amount of sample in the NMR rotor.

we anneal the as-ball-milled samples at high temperature to relax this strain and study the effect of annealing on the cathode cyclability. Both LNNOF25 and LNNOF54 are annealed at 700 °C for 30 min followed by quenching to room temperature and immediately transferred to the antechamber of an Ar-filled glovebox. XRD patterns of the annealed samples (a-LNNOF25 and a-LNNOF54) are presented in Figure 10a,b. After annealing, the lattice parameters decrease from 4.193 to 4.181 Å for LNNOF25 and from 4.181 to 4.168 Å for LNNOF54. Significant peak sharpening is observed for the annealed samples compared with the as-ball-milled ones (Figure 1b,d). For example, the refined full width at half-maximum of the (200) peak of the ball-milled LNNO25 is 1.1141°, whereas that of the a-LNNOF25 is 0.2799°. This finding suggests particle size growth or relaxation of lattice strain at the annealing temperature. The XRD pattern of a-LNNOF25 is well fit by a DRX structural model with the original target composition. In contrast, the XRD pattern of a-LNNOF54 is refined to contain 80.1% of the target phase and 19.9% NiO. No obvious impurity peaks could be identified because NiO has the same rocksalt structure and a similar lattice parameter (4.177 Å)[32] as the target phase (4.1684(4) Å). However, segregated Ni-rich regions were clearly observed using EDS elemental mapping in a-LNNOF54 but not in a-LNNOF25 (Figure S3). Although LiF and the target phase also have highly similar XRD patterns, we do not include LiF as a possible impurity during refinement because the lattice parameter (4.03 Å) is significantly smaller than that observed in the XRD pattern. Instead, we characterize the amount of LiF in both annealed samples using more sensitive ^{19}F ssNMR (Figure 10c,d). While the spectrum of a-LNNOF25 largely retains the broad span of the chemical shift with slightly more contribution from LiF-like environments after annealing, the spectrum of a-LNNOF54 shows significant peak sharpening and shifting toward −204 ppm after annealing. These results indicate that LNNOF25 is stable enough at 700 °C to retain the DRX structure and compositional homogeneity, whereas LNNOF54 is not sufficiently stable. LNNOF54 tends to phase-separate when annealed, which is consistent with the extremely high temperature we compute to be necessary to achieve this high level of fluorination. In addition, the increased ^{19}F NMR signal intensity presumably originates from structural changes in the materials during annealing, leading to a decreased proportion of F nuclei with at least one Ni−F bond (invisible in the spectra). Hence, a possible scenario is that annealing the samples leads to the replacement of high-energy Ni−F bonds with lower-energy Li−F bonds,[9] resulting in a more thermodynamically stable structure. As mentioned earlier, we are unable to quantify the exact proportion of the LiF-like environments in these compounds, due to the strong overlap of the broad NMR signals, which prevents an accurate fit of the data, as well as the absence of the signal from the F nuclei directly bonded to paramagnetic species (here Ni).

The voltage profiles of the two annealed samples for the first 10 cycles are presented in Figure 11a,c. The a-LNNOF25 cathode delivers a first-cycle capacity of ∼200 mAh/g when cycled over the range of 1.5−4.6 V, with a similar voltage profile to the as-ball-milled cathode (Figure 9a). However, its capacity retention is significantly improved, as shown in Figure 11b. Roughly 83% of the original capacity is retained after 20 cycles compared with 40% for the ball-milled LNNOF25. In contrast, the voltage profile of a-LNNOF54 changes substantially compared with that of the as-ball-milled cathode, with its high-voltage plateau region significantly shortened, leading to a limited first-cycle capacity of 133 mAh/g. This reduced capacity is likely associated with the phase segregation observed with XRD and NMR. Nevertheless, a-LNNOF54 retains ∼94% of its original capacity after 20 cycles. The exact reason why the capacity retention improves significantly after

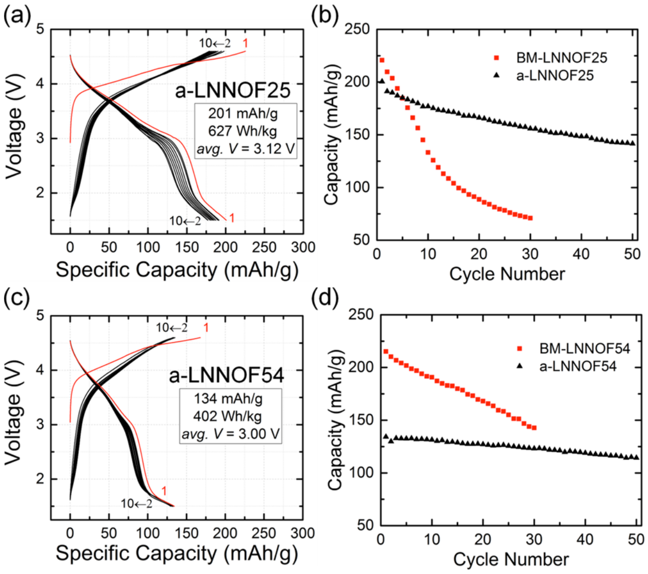

Figure 11. Voltage profiles for the first 10 cycles for (a) a-LNNOF25 and (c) a-LNNOF54. Capacity retention over 50 cycles for (b) a-LNNOF25 and (d) a-LNNOF54. The capacity retention of the ball-milled samples (BM-LNNOF25 and BM-LNNOF54) over 30 cycles is also shown for comparison. The cycling rate for all tests is 20 mA/g.

annealing needs further investigation. Three possible mechanisms are (i) the enhanced crystallinity after annealing leads to better structural retention during cycling, (ii) annealing leads to larger particles and reduced surface area and thus less surface side reactions (e.g., oxygen loss and densification), and (iii) annealing leads to a different cation short-range order from that of the ball-milled samples, resulting in different electrochemical performance.

Given that variations caused by high-energy ball milling and high-temperature annealing might lead to distinct cation short-range orders that are crucial for determining Li transport in these cation-disordered cathode materials,[41] we propose that future investigations combining neutron pair distribution function (PDF), synchrotron PDF, and electrochemical tests are needed to further study the cation short-range order variation obtained through various treatments and the impact of such variation on battery performance.

■ DISCUSSION

Li excess creates percolating Li diffusion pathways in DRX cathodes, but the requirement that it is charge-compensated by high-valent elements reduces the redox-active TM content, leading to a strong dependence on less reversible oxygen redox processes. Fluorination is effective in reducing oxygen loss and voltage hysteresis and improving cycle life. However, the miscibility issue associated with fluorination adds complexity to materials design. In this paper, we demonstrated that a phase diagram of the entire composition space of interest can be computationally constructed to estimate the synthetic accessibility of any given composition. This phase diagram can then be overlaid with design criteria, in this case the Li excess level and TM theoretical capacity, to efficiently identify high-performance oxyfluoride candidates. Following this procedure, we identified two Li−Ni−Nb−O−F DRX compositions, which exhibit much smaller hysteresis than the previously reported pure oxide $Li_{1.3}Ni_{0.27}Nb_{0.43}O_2$.[2] We attribute the significantly reduced charge−discharge voltage hysteresis in both LNNOF25 and LNNOF54 to the increased TM capacity, which is more than double that of the pure oxide.

However, the effect of fluorination is more nuanced than simply increasing the amount of theoretical TM capacity. Fluorination also modifies the voltage profile and redox mechanism.

Even though all compounds rely to some extent on the same $Ni^{2+/3+}$ redox couple, the measured voltage profile of the two studied oxyfluorides differs considerably from that of pure oxides, such as $Li_{1.2}Ni_{1/3}Ti_{1/3}Mo_{2/15}O_2$ or $Li_{1.3}Ni_{0.27}Nb_{0.43}O_2$. One defining feature in the first-charge voltage profiles of the pure oxides is the clear plateau at ∼4.3 V,[1] typically associated with oxygen oxidation. This plateau is absent in LNNOF25 and LNNOF54 and replaced by a sloping voltage, similar to that observed for a few other Li-excess oxyfluorides.[10,13,14] In this region of charge, the Ni K-edge XANES data indicates that Ni oxidation barely contributes to the observed capacity, suggesting oxygen oxidation as a charge compensation mechanism. One may understand the effect of fluorination on the voltage by separately assessing the Li^+ site energy and the electron extraction energy, the sum of which determines the working potential at a given state of charge. It is unlikely that F would modify the energy of the unhybridized O 2p bands responsible for oxygen oxidation,[42] suggesting that the voltage slope results from an increased variation in Li site energy associated with F doping. This mechanism is consistent with previous reports showing the tendency of fluorine to increase the Li extraction voltage via a Li-gettering effect.[12] That is, F ions trap some of the coordinating Li ions to avoid forming high-energy undercoordinated states. Thus, one finding is that fluorination increases the working voltage independent of the redox couple, which to some extent limits the extractable capacity within a given voltage range but may have a beneficial effect in controlling the degree of delithiation and preventing overcharge.

Heavy fluorination also appears to suppress Ni redox. Limited Ni redox has already been observed in a DRX oxide $Li_{1.2}Ni_{1/3}Ti_{1/3}Mo_{2/15}O_2$, as its XANES Ni K-edge spectra indicate that on average Ni is only oxidized to 3+ at the top of charge,[1] in contrast to layered oxides where complete oxidation to Ni^{4+} readily occurs.[43] Two factors contribute to the limited Ni redox in Li-excess DRXs: (i) Li excess and cation disorder create unhybridized O 2p states,[42] leading to facile oxygen oxidation that competes with TM oxidation starting near 4.3 V[44] and (ii) expanded Ni−O bond lengths, that is, less hybridization, in DRXs compared with those in layered materials, lead to lower-lying Ni E_g orbitals and thus an increased Ni redox voltage.[14] In LNNOF54, the maximal average oxidation state of Ni is reduced further to ∼2.7+, even though this compound has a comparable Li-excess level and lattice constant as the non-fluorinated DRX oxides, suggesting that fluorination may be further inhibiting Ni redox. Our cluster expansion results indicate that a majority of Ni ions are directly bonded to at least one F ion in LNNOF54. Given that F ions strongly prefer Li-rich environments, such a population of Ni−F bonds can only be expected when a large amount of fluorine is present. When such bonds do form, as shown for example in $Li_2Mn_{1/2}Ti_{1/2}O_2F$ and $Li_2Mn_{2/3}Nb_{1/3}O_2F$, the presence of TM−F bonds stabilizes the reduced TM state and thus increases the oxidation potential.[14] Therefore, we expect that the Ni−F bonds formed in LNNOF54 lead to even more limited Ni redox than in pure oxides or in lightly fluorinated DRXs.

As a possible remedy for the limited Ni redox, we computationally test the effect of reducing the lattice parameter to counteract the effect of bond stress on suppressing Ni oxidation. From experiments, we observe that the Ni−O bond length change during cycling is smaller in our compounds than in traditional layered Ni oxide cathodes. The Ni−O bond length in LNNOF54 only decreases from ∼2.06 Å in the pristine state to ∼2.01 Å at the top of charge, based on the refinement of the Ni K-edge EXAFS spectra. However, in well-ordered layered oxides, the isolated NiO_6 layer can contract cooperatively, facilitating the formation of short Ni−O bonds characteristic of higher oxidation states of Ni. For example, the Ni−O bond length in a typical layered compound $Li_{1.167}Mn_{0.583}Ni_{0.25}O_2$ shrinks from ∼2.04 Å in the pristine state to ∼1.96 Å in a Ni^{3+} state and even further to 1.89 Å in a Ni^{4+} state.[45] We thus compute the oxidation mechanism of the model $Li_{1.2}Ni_{0.6}Nb_{0.2}O_{1.4}F_{0.6}$ composition while constraining the lattice parameter of the material to 0, 3, and 6% compression with respect to that of the lithiated state. For comparison, the lattice parameter change of a DRX during cycling is typically less than 3%.[1,10] As shown in Figure 12, the accessibility of the $Ni^{2+/3+}$ redox couple is affected by the lattice parameter of the material, with a higher degree of lattice compression enabling a higher conversion of Ni^{2+} to Ni^{3+}. However, the accessible Ni capacity remains below 1 e^-/Ni (see the dashed lines, which denote a hypothetical complete conversion of Ni^{2+} to Ni^{3+}).

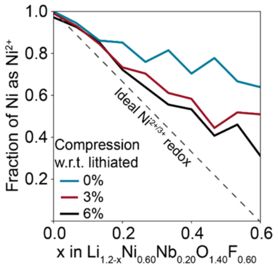

Figure 12. Fraction of Ni computed to remain as Ni^{2+} as a function of charge state with various compressive strain levels in the $Li_{1.2}Ni_{0.6}Nb_{0.2}O_{1.4}F_{0.6}$ model material. The population of Ni^{2+} at each composition and strain level is sampled from an ensemble of 12 partially delithiated structures representative of the structural environments present in a $Li_{1.2}Ni_{0.6}Nb_{0.2}O_{1.4}F_{0.6}$ DRX.

Overall, fluorination increases the theoretical TM capacity, reduces voltage hysteresis, and improves cycle life. Increasing the fluorination level also appears to induce a voltage increase independent of the active redox couple. However, Ni oxidation in a heavily fluorinated DRX is found to be more difficult than in non-fluorinated DRXs, likely due to the increase in the Ni oxidation potential arising from the presence of Ni−F bonds. As a result, Ni oxidation in these materials is limited to less than 1 e^-/Ni. This additional limit on the accessible Ni capacity imposed by fluorination partially counteracts the benefits of using F to increase the total Ni content of the material. These subtle effects of fluorination will have to be taken into account to achieve more precise design of DRX oxyfluoride cathodes. The characterization techniques and the DFT calculations presented in the manuscript focus on the bulk properties of the materials. Future investigation of the impact of surface chemistry and structure, especially upon cycling, is important for elucidating the cyclability difference between disordered rocksalt cathode materials.

■ CONCLUSIONS

We demonstrated the computational design and experimental realization of two Ni-based cation-disordered oxyfluoride cathodes with high capacity and energy density. Both materials exhibit reduced hysteresis and higher energy density than the previously reported oxide, proving the overall effectiveness of fluorination in increasing the transition metal capacity while suppressing the dependence on oxygen redox. Fluorination leads to a voltage increase, likely via a Li-gettering effect. However, heavy fluorination also suppresses Ni redox. Though a high theoretical capacity is expected from the Ni^{2+}/Ni^{4+} redox couple, our findings show that the oxidation state of Ni barely reaches 3+ at full charge. The considerable population of Ni−F bonds predicted by our cluster expansion and Monte Carlo simulations, along with the expanded Ni−O bond lengths and a stronger overlap between nickel and oxygen redox processes, was identified as a possible cause of the limited Ni oxidation. Therefore, the F content in disordered Ni-based rocksalt cathodes needs to be optimized to balance the benefits of increasing the Ni content versus the negative effect of F on the accessibility of the Ni redox reservoir. We show that a post-synthesis annealing treatment can effectively improve the capacity retention for compositions that are close to being thermodynamically stable but lead to phase segregation in highly metastable phases.

■ ASSOCIATED CONTENT

Ⓢ Supporting Information

The Supporting Information is available free of charge on the ACS Publications website at DOI: 10.1021/acs.chemmater.8b05096.

> Additional ^7Li ssNMR results of pristine powder, EXAFS refinement details, TEM-EDS mapping of annealed samples, ex situ XRD and ssNMR (PDF)

■ AUTHOR INFORMATION

Corresponding Author

*E-mail: gceder@berkeley.edu.

ORCID

Huiwen Ji: 0000-0001-8091-9428

Author Contributions

‡These authors contributed equally.

Notes

The authors declare no competing financial interest.

■ ACKNOWLEDGMENTS

This work was supported by Umicore Specialty Oxides and Chemicals and the Assistant Secretary for Energy Efficiency and Renewable Energy, Vehicle Technologies Office of the U.S. Department of Energy under Contract No. DE-AC02-05CH11231 under the Advanced Battery Materials Research (BMR) Program. Work at the Molecular Foundry was supported by the Office of Science, Office of Basic Energy Sciences of the U.S. Department of Energy under Contract No. DE-AC02-05CH11231. Work at Sector 20 in the Advanced Photon Source is supported by the U.S. Department of Energy and the Canadian Light Source. The computational analysis was performed using computational resources sponsored by the Department of Energy's Office of Energy Efficiency and Renewable Energy and located at the National Renewable Energy Laboratory as well computational resources provided by Extreme Science and Engineering Discovery Environment (XSEDE), which was supported by National Science Foundation grant number ACI-1053575. The NMR experimental work reported here made use of the shared facilities of the UCSB MRSEC (NSF DMR 1720256), a member of the Material Research Facilities Network. The authors would also like to thank Jinhyuk Lee for helpful discussions.

■ REFERENCES

(1) Lee, J.; Seo, D.-H.; Balasubramanian, M.; Twu, N.; Li, X.; Ceder, G. A new class of high capacity cation-disordered oxides for rechargeable lithium batteries: Li−Ni−Ti−Mo oxides. *Energy Environ. Sci.* **2015**, *8*, 3255−3265.

(2) Yabuuchi, N.; Takeuchi, M.; Nakayama, M.; Shiiba, H.; Ogawa, M.; Nakayama, K.; Ohta, T.; Endo, D.; Ozaki, T.; Inamasu, T.; Sato, K.; Komaba, S. High-capacity electrode materials for rechargeable lithium batteries: Li_3NbO_4-based system with cation-disordered rocksalt structure. *Proc. Natl. Acad. Sci.* **2015**, *112*, 7650−7655.

(3) Glazier, S. L.; Li, J.; Zhou, J.; Bond, T.; Dahn, J. R. Characterization of Disordered $Li_{(1+x)}Ti_{2x}Fe_{(1-3x)}O_2$ as Positive Electrode Materials in Li-Ion Batteries Using Percolation Theory. *Chem. Mater.* **2015**, *27*, 7751−7756.

(4) Yabuuchi, N.; Nakayama, M.; Takeuchi, M.; Komaba, S.; Hashimoto, Y.; Mukai, T.; Shiiba, H.; Sato, K.; Kobayashi, Y.; Nakao, A.; Yonemura, M.; Yamanaka, K.; Mitsuhara, K.; Ohta, T. Origin of stabilization and destabilization in solid-state redox reaction of oxide ions for lithium-ion batteries. *Nat. Commun.* **2016**, *7*, 13814.

(5) Lee, J.; Urban, A.; Li, X.; Su, D.; Hautier, G.; Ceder, G. Unlocking the potential of cation-disordered oxides for rechargeable lithium batteries. *Science* **2014**, *343*, 519−522.

(6) Urban, A.; Lee, J.; Ceder, G. The Configurational Space of Rocksalt-Type Oxides for High-Capacity Lithium Battery Electrodes. *Adv. Energy Mater.* **2014**, *4*, 1400478.

(7) Kan, W. H.; Chen, D.; Papp, J. K.; Shukla, A. K.; Huq, A.; Brown, C. M.; McCloskey, B. D.; Chen, G. Unravelling Solid-State Redox Chemistry in $Li_{1.3}Nb_{0.3}Mn_{0.4}O_2$ Single-Crystal Cathode Material. *Chem. Mater.* **2018**, *30*, 1655−1666.

(8) Du, K.; Zhu, J.; Hu, G.; Gao, H.; Li, Y.; Goodenough, J. B. Exploring reversible oxidation of oxygen in a manganese oxide. *Energy Environ. Sci.* **2016**, *9*, 2575−2577.

(9) Richards, W. D.; Dacek, S. T.; Kitchaev, D. A.; Ceder, G. Fluorination of Lithium-Excess Transition Metal Oxide Cathode Materials. *Adv. Energy Mater.* **2018**, *8*, 1701533.

(10) Lee, J.; Papp, J. K.; Clément, R. J.; Sallis, S.; Kwon, D.-H.; Shi, T.; Yang, W.; McCloskey, B. D.; Ceder, G. Mitigating oxygen loss to improve the cycling performance of high capacity cation-disordered cathode materials. *Nat. Commun.* **2017**, *8*, 981.

(11) Chen, R.; Ren, S.; Knapp, M.; Wang, D.; Witter, R.; Fichtner, M.; Hahn, H. Disordered Lithium-Rich Oxyfluoride as a Stable Host for Enhanced Li^+ Intercalation Storage. *Adv. Energy Mater.* **2015**, *5*, 1401814.

(12) Kitchaev, D. A.; Lun, Z.; Richards, W. D.; Ji, H.; Clément, R. J.; Balasubramanian, M.; Kwon, D.-H.; Dai, K.; Papp, J. K.; Lei, T.; McCloskey, B. D.; Yang, W.; Lee, J.; Ceder, G. Design principles for high transition metal capacity in disordered rocksalt Li-ion cathodes. *Energy Environ. Sci.* **2018**, *11*, 2159−2171.

(13) House, R. A.; Jin, L.; Maitra, U.; Tsuruta, K.; Somerville, J. W.; Förstermann, D. P.; Massel, F.; Duda, L.; Roberts, M. R.; Bruce, P. G. Lithium manganese oxyfluoride as a new cathode material exhibiting oxygen redox. *Energy Environ. Sci.* **2018**, *11*, 926−932.

(14) Lee, J.; Kitchaev, D. A.; Kwon, D.-H.; Lee, C.-W.; Papp, J. K.; Liu, Y.-S.; Lun, Z.; Clément, R. J.; Shi, T.; McCloskey, B. D.; Guo, J.; Balasubramanian, M.; Ceder, G. Reversible Mn^{2+}/Mn^{4+} double redox in lithium-excess cathode materials. *Nature* **2018**, *556*, 185−190.

(15) Hung, I.; Zhou, L.; Pourpoint, F.; Grey, C. P.; Gan, Z. Isotropic high field NMR spectra of Li-ion battery materials with anisotropy> 1 MHz. *J. Am. Chem. Soc.* **2012**, *134*, 1898−1901.

(16) Kelly, S. D.; Hesterberg, D.; Ravel, B. Analysis of Soils and Minerals Using X-ray Absorption Spectroscopy. In *Methods of Soil Analysis Part 5—Mineralogical Methods*; Ulery, A. L., Drees, R. L., Eds.; SSSA: Madison, WI, 2008; Chapter 14, pp 387−463.

(17) Ravel, B.; Newville, M. ATHENA,ARTEMIS,HEPHAESTUS: data analysis for X-ray absorption spectroscopy usingIFEFFIT. *J. Synchrotron Radiat.* **2005**, *12*, 537−541.

(18) Rehr, J. J.; Albers, R. C. Theoretical approaches to x-ray absorption fine structure. *Rev. Mod. Phys.* **2000**, *72*, 621.

(19) Kresse, G.; Furthmüller, J. Efficient iterative schemes for *ab initio* total-energy calculations using a plane-wave basis set. *Phys. Rev. B* **1996**, *54*, 11169.

(20) Kresse, G.; Furthmüller, J. Efficiency of ab-initio total energy calculations for metals and semiconductors using a plane-wave basis set. *Comput. Mater. Sci.* **1996**, *6*, 15−50.

(21) Blöchl, P. E. Projector augmented-wave method. *Phys. Rev. B* **1994**, *50*, 17953.

(22) Perdew, J. P.; Burke, K.; Ernzerhof, M. Generalized Gradient Approximation Made Simple. *Phys. Rev. Lett.* **1996**, *77*, 3865.

(23) Dudarev, S. L.; Botton, G. A.; Savrasov, S. Y.; Humphreys, C. J.; Sutton, A. P. Electron-energy-loss spectra and the structural stability of nickel oxide: An LSDA+ U study. *Phys. Rev. B* **1998**, *57*, 1505.

(24) Jain, A.; Hautier, G.; Moore, C. J.; Ong, S. P.; Fischer, C. C.; Mueller, T.; Persson, K. A.; Ceder, G. A high-throughput infrastructure for density functional theory calculations. *Comput. Mater. Sci.* **2011**, *50*, 2295−2310.

(25) Kitchaev, D. A.; Peng, H.; Liu, Y.; Sun, J.; Perdew, J. P.; Ceder, G. Energetics of MnO_2 polymorphs in density functional theory. *Phys. Rev. B* **2016**, *93*, No. 045132.

(26) Zhang, Y.; Kitchaev, D. A.; Yang, J.; Chen, T.; Dacek, S. T.; Sarmiento-Pérez, R. A.; Marques, M. A. L.; Peng, H.; Ceder, G.; Perdew, J. P.; Sun, J. Efficient first-principles prediction of solid stability: Towards chemical accuracy. *npj Comput. Mater.* **2018**, *4*, 9.

(27) Heyd, J.; Scuseria, G. E.; Ernzerhof, M. Hybrid functionals based on a screened Coulomb potential. *J. Chem. Phys.* **2003**, *118*, 8207−8215.

(28) Ong, S. P.; Richards, W. D.; Jain, A.; Hautier, G.; Kocher, M.; Cholia, S.; Gunter, D.; Chevrier, V. L.; Persson, K. A.; Ceder, G. Python Materials Genomics (pymatgen): A robust, open-source python library for materials analysis. *Comput. Mater. Sci.* **2013**, *68*, 314−319.

(29) Sanchez, J. M.; Ducastelle, F.; Gratias, D. Generalized cluster description of multicomponent systems. *Phys. A* **1984**, *128*, 334−350.

(30) Tepesch, P. D.; Garbulsky, G. D.; Ceder, G. Model for Configurational Thermodynamics in Ionic Systems. *Phys. Rev. Lett.* **1995**, *74*, 2272.

(31) Nelson, L. J.; Hart, G. L. W.; Zhou, F.; Ozoliņš, V. Compressive sensing as a paradigm for building physics models. *Phys. Rev. B* **2013**, *87*, No. 035125.

(32) Wakabayashi, I.; Kobayashi, H.; Nagasaki, H.; Minomura, S. The effect of pressure on the lattice parameters Part I. PbS and PbTe Part II. Gd, NiO, and α-MnS. *J. Phys. Soc. Jpn.* **1968**, *25*, 227−233.

(33) Clément, R. J.; Kitchaev, D.; Lee, J.; Ceder, G. Short-range order and unusual modes of nickel redox in a fluorine-substituted disordered rocksalt oxide lithium-ion cathode. *Chem. Mater.* **2018**, *30*, 6945−6956.

(34) Vassilaras, P.; Kwon, D.-H.; Dacek, S. T.; Shi, T.; Seo, D.-H.; Ceder, G.; Kim, J. C. Electrochemical properties and structural evolution of O3-type layered sodium mixed transition metal oxides with trivalent nickel. *J. Mater. Chem. A* **2017**, *5*, 4596−4606.

(35) Shannon, R. D. Revised effective ionic radii and systematic studies of interatomic distances in halides and chalcogenides. *Acta Crystallogr., Sect. A: Found. Adv.* **1976**, *32*, 751−767.

(36) Balasubramanian, M.; McBreen, J.; Davidson, I. J.; Whitfield, P. S.; Kargina, I. In situ X-ray absorption study of a layered manganese-chromium oxide-based cathode material. *J. Electrochem. Soc.* **2002**, *149*, A176−A184.

(37) Urban, A.; Abdellahi, A.; Dacek, S.; Artrith, N.; Ceder, G. Electronic-structure origin of cation disorder in transition-metal oxides. *Phys. Rev. Lett.* **2017**, *119*, 176402.

(38) Demourgues, A.; Gautier, L.; Chadwick, A. V.; Delmas, C. EXAFS study of the Jahn-Teller distortion in layered nickel oxyhydroxide. *Nucl. Instrum. Methods Phys. Res., Sect. B* **1997**, *133*, 39−44.

(39) Assat, G.; Foix, D.; Delacourt, C.; Iadecola, A.; Dedryvère, R.; Tarascon, J.-M. Fundamental interplay between anionic/cationic redox governing the kinetics and thermodynamics of lithium-rich cathodes. *Nat. Commun.* **2017**, *8*, 2219.

(40) Dogan, F.; Long, B. R.; Croy, J. R.; Gallagher, K. G.; Iddir, H.; Russell, J. T.; Balasubramanian, M.; Key, B. Re-entrant lithium local environments and defect driven electrochemistry of Li- and Mn-rich Li-ion battery cathodes. *J. Am. Chem. Soc.* **2015**, *137*, 2328−2335.

(41) Ji, H.; Urban, A.; Kitchaev, D. A.; Kwon, D.-H.; Artrith, N.; Ophus, C.; Huang, W.; Cai, Z.; Shi, T.; Kim, J. C.; Kim, H.; Ceder, G. Hidden structural and chemical order controls lithium transport in cation-disordered oxides for rechargeable batteries. *Nat. Commun.* **2019**, *10*, 592.

(42) Seo, D.-H.; Lee, J.; Urban, A.; Malik, R.; Kang, S.; Ceder, G. The structural and chemical origin of the oxygen redox activity in layered and cation-disordered Li-excess cathode materials. *Nat. Chem.* **2016**, *8*, 692.

(43) Yoon, W.-S.; Balasubramanian, M.; Chung, K. Y.; Yang, X.-Q.; McBreen, J.; Grey, C. P.; Fischer, D. A. Investigation of the Charge Compensation Mechanism on the Electrochemically Li-Ion Deintercalated $Li_{1-x}Co_{1/3}Ni_{1/3}Mn_{1/3}O_2$ Electrode System by Combination of Soft and Hard X-ray Absorption Spectroscopy. *J. Am. Chem. Soc.* **2005**, *127*, 17479−17487.

(44) Abdellahi, A.; Urban, A.; Dacek, S.; Ceder, G. The effect of cation disorder on the average Li intercalation voltage of transition-metal oxides. *Chem. Mater.* **2016**, *28*, 3659−3665.

(45) Muhammad, S.; Kim, H.; Kim, Y.; Kim, D.; Song, J. H.; Yoon, J.; Park, J.-H.; Ahn, S.-J.; Kang, S.-H.; Thackeray, M. M.; Yoon, W.-S. Evidence of reversible oxygen participation in anomalously high capacity Li- and Mn-rich cathodes for Li-ion batteries. *Nano Energy* **2016**, *21*, 172−184.

DOI: 10.1021/acs.chemmater.8b05096